Land surface albedo bias in climate models and its association with tropical rainfall

Xavier J. Levine,[1] and William R. Boos[1]

The influence of land surface albedo on tropical precipitation has been widely appreciated for decades, but bias in the representation of surface albedo in weather and climate models has been studied much less than bias in sea surface temperature or soil moisture. This study shows that CMIP5 simulations of the late 20th century exhibit large multi-model mean bias and intermodel variability in surface broadband shortwave albedo. Intermodel variability in surface albedo is coherent on global scales and correlates with intermodel variability of precipitation over large parts of the tropics. Although enhanced rainfall would be expected to reduce soil albedo, evidence is presented in support of the alternate hypothesis that intermodel albedo variability instead causes intermodel precipitation variability. Further study is needed to elucidate the cause of surface albedo bias in individual models, but these results suggest that reducing that bias will improve simulations of low-latitude precipitation.

1. Introduction

Since the seminal work of *Charney* [1975], surface albedo has been recognized as a major influence on climate over a wide range of timescales, from sub-seasonal to orbital. On centennial timescales, surface albedo changes in boreal regions may have helped foster global glaciation, as forests changed to grasslands during the initial cooling of glacial onset [*de Noblet et al.*, 1996; *Schurgers et al.*, 2007]. Similarly, the North African humid period during the mid-Holocene likely required a substantial surface albedo reduction in the Sahara [*Laval and Picon*, 1986; *Kutzbach et al.*, 1996; *de Noblet-Ducoudré et al.*, 2000; *Bonfils et al.*, 2001; *Vamborg et al.*, 2011] and perhaps also in boreal regions [*Foley et al.*, 1994]. These albedo changes, in turn, require changes in vegetation cover [*Xue and Shukla*, 1993; *Claussen and Gayler*, 1997], soil organic matter content [*Knorr and Schnitzler*, 2006], or soil moisture content [*Walker and Rowntree*, 1977]. On decadal timescales, regional climate variability can be amplified by albedo changes, as has been suggested for multi-decadal Sahel drought [*Charney et al.*, 1977; *Zeng et al.*, 1999; *Vamborg et al.*, 2014]. Surface albedo may even influence sub-seasonal variability: the skill of weather forecasts over India has been shown to be influenced by model representation of surface albedo [*Kumar et al.*, 2014]. Anthropogenic tropical deforestation has been argued to increase surface brightness and thus reduce precipitation [*Dirmeyer and Shukla*, 1994], in particular over the Amazon basin [*Costa and Foley*, 2000; *Berbet and Costa*, 2003] and West Africa [*Kitoh et al.*, 1988; *Zheng and Eltahir*, 1998]. Conversely, reforestation and surface darkening might amplify global warming [*Bonan et al.*, 1992; *Betts*, 2000].

Despite the known importance of surface albedo, its representation in comprehensive global climate models and its influence on simulated climate remain poorly characterized. Some outstanding issues have been recognized: for instance, large intermodel albedo variability is found in boreal regions during winter and spring due to variability in snow and vegetation cover [*Wang et al.*, 2016; *Li et al.*, 2016]. The representation of tropical surface albedo variability in dry zones has been found to affect simulations of regional climate [*Sud and Fennessy*, 1982], especially in North Africa and the Middle East [*Knorr et al.*, 2001; *Samson et al.*, 2016]. Yet we lack a global assessment of surface albedo bias in climate models and an understanding of the influence of this bias on simulated regional climate. Such an assessment may be particularly important during boreal summer in regions where thermal maxima lie over land [*Nie et al.*, 2010] and thus are highly sensitive to land surface properties. Here, we document surface albedo bias and intermodel variability in the Coupled Model Intercomparison Project Phase 5 (CMIP5), then present results consistent with the hypothesis that intermodel variations in albedo cause intermodel variations in regional precipitation.

2. Data

Here surface albedo and precipitation are compared across simulations from 47 CMIP5 models [*Taylor et al.*, 2012] listed in Supplementary Table S1. All simulations are single member hindcasts of the historical period (1850-2005; historical_r1i1p1); here we only use data between 1985 and 2004 to allow comparison with satellite-derived observational products. We use monthly mean precipitation together with both upwelling and downwelling surface broadband shortwave radiative flux. We define a monthly mean surface broadband shortwave albedo (hereafter referred to as "albedo") as the ratio of monthly mean surface upwelling to monthly mean surface downwelling shortwave radiative flux. Monthly means are combined into seasonal means, e.g. June-Sept. (JJAS) for boreal summer and Dec.-March (DJFM) for boreal winter. All model output is re-gridded to $1^\circ \times 1^\circ$ grid.

Model albedo is compared to that estimated from the Energy Balanced And Filled (EBAF) output of the Clouds and the Earth's Radiant Energy System (CERES) mission. CERES EBAF-Surface_Ed2.8 (hereafter CERES) derives broadband shortwave and longwave fluxes at the surface from a radiative transfer calculation based on top-of-atmosphere (TOA) shortwave and longwave radiances obtained from three satellite platforms — EOS Terra, EOS Aqua, and Suomi National Polar-orbiting Partnership (S-NPP) — as well as cloud properties derived from these and other platforms (e.g. the Moderate Resolution Imaging Spectroradiometer [MODIS] and the Visible and Infrared Sounder [VIRS] missions) [*Kato et al.*, 2013]. CERES provides monthly-mean outputs on a $1^\circ \times 1^\circ$ grid from March, 2000 to February 2016. That is, CERES albedo can be analyzed over 16 boreal summers and 15 boreal winters, compared to 20 seasons in CMIP5. To ease comparison with CMIP5 output, interannual standard deviations and multi-year means of albedo are computed from CERES outputs following the same procedures described above for CMIP5.

[1]Department of Geology and Geophysics, Yale University, New Haven, Connecticut, USA.

0094-8276/17/$5.00

3. Results

3.1. CMIP5 bias and intermodel scatter

A well-known aspect of surface albedo is its large spatial variability: during boreal summer the CMIP5 multi-model mean albedo shows intense contrast between dark tropical rainforests, where albedo can be as low as 0.1, and bright subtropical and polar deserts, where albedo often exceeds 0.4 (Fig. 1a). Although this spatial pattern is broadly consistent with observations, the multi-model mean albedo shows significant bias over land when compared with CERES (Fig. 1b). In some regions the magnitude of the albedo bias exceeds 0.1, which implies a bias in absorbed surface shortwave radiation on the order of tens of W m^{-2} (comparison with MODIS surface albedo yields a highly similar bias, Supplementary Fig. S1). During boreal summer, a large negative bias exists over the Sahara and Arabian deserts; smaller negative bias is also found over large swathes of the eastern U.S., the Amazon basin, and Europe (Fig. 1b). Positive bias exists over nearly all other land regions. Oceans show comparatively weak but nonzero bias.

During boreal winter, snow cover causes large surface brightening in the northern extratropics and in tropical highlands (Fig. 1c), which are regions of large bias in the multi-model mean (Fig. 1d). While snow cover bias in models has been shown to be large and to influence global climate [e.g. *Randall et al.*, 1994; *Qu and Hall*, 2006], we henceforth focus on the less well-known biases found during boreal summer. Although smaller in magnitude than the wintertime snow-related albedo bias, the albedo bias over low-latitude land will influence the land surface enthalpy fluxes that control the time-mean overturning circulations that organize tropical precipitation [e.g. *Charney*, 1975; *Xue and Shukla*, 1993].

The intermodel spread of boreal summer albedo is similar in magnitude to the multi-model mean bias in many locations (Fig. 2a). To first-order, intermodel variability increases with albedo, being largest over polar regions, subtropical deserts, and highlands, and smallest over forests and oceans. The local intermodel standard deviation varies between 10-25% of the multi-model mean albedo (Fig. 2b); relative to its local value, albedo variability over snow-free regions is large over tropical vegetated regions and midlatitudes, and lowest over deserts. Relative albedo variability is substantial over oceans, where the intermodel standard deviation is 15% of the multi-model mean.

Intermodel variance of boreal summer albedo is much larger than the multi-model mean interannual variance of that albedo (Fig. 2a, c, e), with the latter negligible nearly everywhere except over elevated terrain and polar regions where variations in snow and ice cover can cause large albedo variability. The small interannual variability of albedo in CMIP5 simulations is broadly consistent with the small interannual variability of observed albedo (Fig. 2d). In contrast, interannual variability in precipitation is comparable to intermodel variability in precipitation (Fig. 2f). This is one piece of evidence supporting the hypothesis that model albedo bias is not caused by precipitation bias. Specifically, if a precipitation variation δP caused a surface albedo variation $\delta\alpha$, we would expect to be able to write the latter as a function of the former. Since the historical CMIP5 simulations do not employ dynamic vegetation [see Table 3 in *Taylor et al.*, 2009], this function will not depend on the time scale of the variation as long as that time scale is seasonal or longer (i.e. the time needed for adjustment of soil moisture or leaf area). So unless the function relating $\delta\alpha$ to δP is strongly nonlinear,

$$\frac{\delta\alpha_{\text{interannual}}}{\delta\alpha_{\text{intermodel}}} \approx \frac{\delta P_{\text{interannual}}}{\delta P_{\text{intermodel}}} \tag{1}$$

where the subscript denotes the type of variation. Since the left-hand side of (1) is much smaller than the right-hand side in CMIP5 (Fig. 2e, f), this implies that model precipitation bias does not cause model albedo bias.

To reveal spatial patterns of intermodel albedo variability, we perform a principal component analysis (PCA). We restrict the domain of analysis to land within 60°S-60°N to exclude polar snow-covered regions. The first and second modes of variability, PC1 and PC2, explain 35% and 17% of intermodel variance, respectively, while higher modes explain less than 7% each. Maps of the empirical orthogonal functions (EOFs) corresponding to the first two modes highlights geographically distinct patterns. EOF1 represents albedo variation over most land regions excluding the Sahara and Middle East (Fig. 3a), while EOF2 primarily represents variations over the Sahara and Arabian deserts (Fig. 3b). Broadly, the first and second modes represent regions with and without vegetation cover, respectively. We henceforth focus mostly on EOF1 since it accounts for the larger fraction of intermodel albedo variance, but recognize that albedo bias over the Sahara may be of great importance for Sahel rainfall [e.g. *Charney*, 1975].

3.2. Precipitation-albedo association

The large intermodel variability of albedo and its coherence on planetary scales may have consequences for simulated low-latitude precipitation, given that surface albedo is known to influence precipitating tropical circulations [e.g. *Charney*, 1975; *Eltahir*, 1996; *Zeng and Neelin*, 1999]. To gauge the association between albedo α and precipitation P, we define a coupling index

$$I(P,\alpha) = \sigma(\alpha)\,\frac{\partial P}{\partial \alpha}, \tag{2}$$

where $\sigma(\alpha)$ is the intermodel standard deviation of α and $\partial_\alpha P$ is obtained from linear regression of P on α. A similar measure was used to assess the association of soil moisture with precipitation [*Dirmeyer*, 2011], and I simply scales the regression coefficient by the intermodel variability in α.

When the local values of boreal summer P and α are used to compute I at every location, the strongest local association between continental precipitation and albedo is found over India, the Sahel, and eastern China (Fig. 4a). Over land, precipitation is almost always anti-correlated with albedo, consistent with the idea of brighter surfaces disfavoring local continental precipitation [e.g., *Charney*, 1975].

But given the strong spatial correlations in intermodel albedo variations (e.g. Fig. 3a), a strong local correlation between variations in precipitation and albedo does not necessarily imply local causation. Indeed, it would be surprising if local ocean albedo variations in the West Pacific caused the increase in equatorial central Pacific rainfall seen in Fig. 4a, given the small magnitude of ocean albedo variations (e.g. Fig. 2a). So we compare this distribution of I, which was computed from local values of α and P, to another version computed using the intermodel albedo anomaly that projects on EOF1, $I(P, \langle\alpha_1\rangle)$. Here, $\langle(.)\rangle$ is an area-weighted average over all land regions 60°S-60°N, and α_1 is the intermodel albedo anomaly that projects on the first EOF, i.e. $\alpha_1 = \mathrm{PC1}(\alpha) \times \mathrm{EOF1}(\alpha)$. The association of P with $\langle\alpha_1\rangle)$ is roughly similar to the local association: e.g., strong association exists over large parts of South and East Asia (Fig. 4b). The tropical Pacific association is also similar, though here more clearly represents a northward shift in the intertropical convergence zone (ITCZ) over much of the Pacific in models having high albedo of vegetated land. Also,

$I(P, \langle\alpha_1\rangle)$ is weaker than the local coupling index $I(P, \alpha)$ over central India and the Sahel. The difference over the Sahel is not surprising, because albedo EOF1 has low magnitude over northern Africa, where albedo variations project more strongly onto EOF2. Similar results are obtained when the association of P and α is assessed using a maximum covariance analysis, as shown in Supplementary Fig. S2.

These associations are generally consistent with the hypothesis that brighter land surfaces cause a reduction in continental precipitation. Despite large regional shifts in precipitation, we do not find a significant meridional shift in precipitation in the zonal mean, due to a large cancellation in the meridional shift of regional ITCZs. This suggests either that vegetated land albedo does not strongly influence the zonal-mean column-integrated atmospheric energy budget [*Chiang and Bitz*, 2005; *Broccoli et al.*, 2006; *Kang et al.*, 2008; *Donohoe et al.*, 2013], or that there are compensating changes in the zonal-mean gross moist stability or in zonal-mean feedbacks (e.g. due to clouds). This contrasts with the precipitation shifts shown to be caused directly by surface albedo changes in cloud-free regions such as the Sahara [e.g. *Charney*, 1975; *Boos and Korty*, 2016].

The fraction of intermodel precipitation variance that is associated with intermodel albedo variations is largest in South Asia, the southern Indian Ocean and Australia, and the East Pacific ITCZ region, consistent with the strong regression coefficients seen in those regions (Fig. 4a, b). The square of the correlation coefficient nears or reaches 0.5 in individual grid cells in those regions (Fig. 3S a), and is about 0.5 when precipitation averaged over Continental South Asia ($60° - 180°$E, $5° - 45°$N; land regions only) and PC1 albedo are correlated (see Fig. 3S b for details). This confirms that the coupling indices discussed above describe a large fraction of intermodel variations in precipitation.

3.3. Precipitation sensitivity to albedo in CESM

Our regression analysis cannot separate the local and remote associations between albedo and precipitation due to the planetary-scale coherence of intermodel albedo variability, nor it can establish causation between albedo and precipitation variations. This is problematic since either direction of causation — increased land rainfall driving lower albedo or lower albedo modifying rainfall — seems physically plausible. To address this problem, we simulate the precipitation response to a global albedo anomaly imposed in vegetated regions.

We use the Community Earth System Model (CESM) version 1.0.4 from the National Center for Atmospheric Research (NCAR). This model consists of a global atmospheric model (the Community Atmosphere Model, CAM, version 5) coupled to a dynamical ocean (the Parallel Ocean Program, version 2), sea ice (CICE4) and land ice (GLC), as well as interacting with a comprehensive land model (CLM) controlling surface properties over ice-free regions. In a control simulation, we integrate CESM with Earth's present-day radiative forcings and boundary conditions (B2000 configuration), with horizontal resolution of $0.9° \times 1.25°$ and 26 vertical levels for the atmosphere, and a nominal ocean resolution of $1°$. This control is run for 65 years with output averaged over the last 55 years. In a perturbation simulation we run CESM with modified land albedo: over regions where the direct beam albedo is lower than 0.15, both direct and diffuse albedos are set to 0.01. This modifies the CESM broadband surface albedo, which we refer to as α_{CESM}, to be darker in vegetated regions in a spatial pattern broadly resembling albedo EOF1 (compare Figs. 3a and 4c).

To compare the precipitation response to this CESM albedo anomaly with the association between intermodel precipitation and albedo variations in CMIP5, we define a coupling index

$$I(P, \langle\alpha_{\mathrm{CESM}}\rangle) = \sigma(\langle\alpha_1\rangle)\,\frac{\Delta P}{\Delta\,\langle\alpha_{\mathrm{CESM}}\rangle} \tag{3}$$

where Δ signifies a difference between the control and perturbation CESM integrations. To facilitate comparison with the CMIP5 results, we construct (3) by scaling the CESM sensitivity by the standard deviation of albedo EOF1 obtained from the CMIP5 models, $\sigma(\langle\alpha_1\rangle)$. This coupling index has many similarities to the coupling index between precipitation and albedo EOF1 in the CMIP5 simulations, $I(P, \langle\alpha_1\rangle)$, as seen in Figs. 4d with 4b. In particular, brighter albedo over vegetated regions decreases precipitation over South Asia and Australia, but increases rainfall over the equatorial East Indian Ocean; similarity is particularly strong over the East Pacific, where the ITCZ shifts poleward as land albedo brightens, and it is remarkable that the CESM response has a magnitude that is overall similar to that of the albedo-related precipitation variations seem in CMIP5. Substantial differences also exist between the CMIP5 associations and the CESM response, particularly in the Sahel and Central Africa. Yet the CESM result broadly supports our hypothesis that intermodel differences in land albedo cause intermodel precipitation variations in CMIP5.

4. Discussion: causes of albedo bias

Understanding the cause of albedo bias and intermodel albedo variability is challenging due to both model complexity and lack of detailed output about the radiative properties of the surface and atmosphere. Nevertheless, the near-global coherence of intermodel albedo variations over continental regions and their weak interannual variability suggest that model albedo variations are unlikely to be driven by a quantity with large spatial or interannual variability, such as precipitation. Instead, a spatially homogeneous quantity might cause spatially coherent albedo variability, for instance by modifying the atmospheric radiative properties. For example, tropospheric water vapor, which has higher homogeneity across the tropics than precipitation, preferentially absorbs shortwave flux in the near-infrared (IR) [*Pierrehumbert*, 2010]; since vegetated surfaces have lower albedo in the visible than in the near-IR [*Houldcroft et al.*, 2009], greater tropospheric water vapor in a model could reduce broadband surface albedo. Another potential source of albedo variability is the illumination angle [*Song*, 1998], particularly the relative contribution of diffuse and direct shortwave flux reaching the surface, because white-sky (i.e. diffuse) albedo in MODIS is typically 10% to 15% larger than black sky (i.e. direct local noon) albedo [*Houldcroft et al.*, 2009]. Water vapor and other species (e.g. aerosols) can thus bias broadband surface albedo by absorbing or scattering shortwave flux. Clouds can amplify these biases, with reflection between surface and clouds substantially increasing the path length over which extinction occurs [*Ambach*, 1974].

We obtained a rough estimate of the influence of these processes on broadband shortwave albedo through some idealized calculations conducted with the Fu-Liou radiative transfer code (available at https://www-cave.larc.nasa.gov/cgi-bin/fuliou/runfl.cgi as part of the CERES/ARM Validation Experiment; see *Fu and Liou* [1993] for details). Using typical land surfaces (e.g. mixed forest, woody savannah, grassland) as a lower boundary and typical tropical conditions (e.g. temperature and atmospheric constituents), we estimated changes in the broadband shortwave albedo in a cloud-free atmosphere due to changing tropospheric water vapor and solar zenith angle. Land surface albedo typically increased by 5%-20% of its original value when water vapor was reduced from its tropical-mean value to near zero, while it increased by up to 20% when solar radiation was changed from direct beam at noon to isotropic, diffuse illumination. Since the CMIP5 intermodel variations in tropical-mean specific humidity and illumination angle are expected to be much smaller than these limiting cases, it seems unlikely that these factors could cause the large intermodel albedo variations found here (the intermodel standard deviation exceeds 20% over many land regions, e.g. Fig. 2b). On the other hand, intermodel variations in shortwave absorption or scattering might be important in regions where albedo has a lower intermodel variability relative to its mean (e.g. deserts).

An alternate hypothesis is that intermodel albedo variability is caused by different prescriptions of soil and vegetation properties among models. Models use different distributions of plant functional types (PFTs) when representing identical land surfaces [e.g., *de Noblet-Ducoudré et al.*, 2012], and bias in PFT distributions has been shown to produce surface albedo bias of up to 25% [*Matthes et al.*, 2016]. Models also differ in the complexity of how their vegetation model interacts with radiation; for instance, differences in canopy shortwave flux absorption could bias surface albedo even if soil albedo and PFTs are unbiased [e.g. *Betts*, 2000]. Differences in soil moisture and organic matter may also lead to albedo bias if organic matter or soil moisture is either set dynamically or not consistently prescribed among models [e.g. *Levis et al.*, 2004; *Vamborg et al.*, 2011]. In summary, while albedo can be influenced by intermodel variations in climatological mean quantities that alter shortwave scattering and absorption, we suggest that albedo bias in individual models is more likely caused by prescription of surface properties such as PFTs or canopy radiative transfer.

5. Conclusions

The CMIP5 intermodel variations of surface albedo found here are spatially coherent over large swathes of the subtropics and midlatitudes, and are not caused by snow cover variations. These intermodel albedo variations correlate with intermodel precipitation variability in many low-latitude regions; brighter vegetated surfaces on global scales are associated with less precipitation over most tropical land and a northward shift of the East Pacific ITCZ. While a reduction in land precipitation is expected to result from brighter land albedo [e.g. *Charney*, 1975], the mechanism tying albedo to remote ITCZ shifts remains unclear. Nevertheless, by simulating the response to reduced albedo over vegetated regions in a comprehensive climate model, we find evidence that global-scale albedo variations over vegetated land can cause precipitation changes of the pattern and magnitude seen in CMIP5. The precipitation-albedo association is strong in CMIP5, with these variables having an R^2 of 0.6 when first averaged over low-land South Asia.

We argued that differing representations of vegetation and soil properties are a likely cause of these albedo variations, with variations in mean climate variables such as water vapor, soil moisture, aerosols, and clouds playing a lesser role. The lack of spectrally resolved radiative flux output in the CMIP5 archive unfortunately prevents quantification of these effects. Although further work is needed to determine whether remediating albedo bias in individual models will reduce precipitation bias, this seems a promising approach for addressing longstanding biases in tropical rainfall, such as the dry bias that has persisted over continental India through generations of climate models [e.g. *Sperber et al.*, 2013].

Acknowledgments. We acknowledge Office of Naval Research award N00014-15-1-2531 and National Science Foundation awards AGS-1253222 and AGS-1515960. X. Levine thanks Ravi Shekhar for many helpful discussions.

References

Ambach, W. (1974), The influence of cloudiness on the net radiation balance of a snow surface with high albedo, *Journal of Glaciology*, *13*(67), 73–84.

Berbet, M. L. C., and M. H. Costa (2003), Climate change after tropical deforestation: seasonal variability of surface albedo and its effects on precipitation change, *Journal of climate*, *16*(12), 2099–2104.

Betts, R. A. (2000), Offset of the potential carbon sink from boreal forestation by decreases in surface albedo, *Nature*, *408*(6809), 187–190.

Bonan, G. B., D. Pollard, and S. L. Thompson (1992), Effects of boreal forest vegetation on global climate, *Nature*, *359*, 716–718.

Bonfils, C., N. de Noblet-Ducoudré, P. Braconnot, and S. Joussaume (2001), Hot desert albedo and climate change: Mid-Holocene monsoon in North Africa, *Journal of Climate*, *14*(17), 3724–3737.

Boos, W. R., and R. L. Korty (2016), Regional energy budget control of the intertropical convergence zone and application to mid-Holocene rainfall, *Nature Geoscience*, *9*(12), 892–897.

Broccoli, A. J., K. A. Dahl, and R. J. Stouffer (2006), Response of the ITCZ to Northern Hemisphere cooling, *Geophysical Research Letters*, *33*(1).

Charney, J., W. J. Quirk, S.-H. Chow, and J. Kornfield (1977), A comparative study of the effects of albedo change on drought in semi-arid regions, *Journal of the Atmospheric Sciences*, *34*(9), 1366–1385.

Charney, J. G. (1975), Dynamics of deserts and drought in the Sahel, *Quarterly Journal of the Royal Meteorological Society*, *101*(428), 193–202.

Chiang, J. C. H., and C. M. Bitz (2005), Influence of high latitude ice cover on the marine Intertropical Convergence Zone, *Climate Dynamics*, *25*(5), 477–496.

Claussen, M., and V. Gayler (1997), The greening of the Sahara during the mid-Holocene: results of an interactive atmosphere-biome model, *Global Ecology and Biogeography Letters*, pp. 369–377.

Costa, M. H., and J. A. Foley (2000), Combined effects of deforestation and doubled atmospheric CO2 concentrations on the climate of Amazonia, *Journal of Climate*, *13*(1), 18–34.

de Noblet, N. I., I. C. Prentice, S. Joussaume, D. Texier, A. Botta, and A. Haxeltine (1996), Possible role of atmosphere-biosphere interactions in triggering the Last Glaciation, *Geophysical Research Letters*, *23*(22), 3191–3194.

de Noblet-Ducoudré, N., M. Claussen, and I. C. Prentice (2000), Mid-Holocene greening of the Sahara: first results of the GAIM 6000 year BP experiment with two asynchronously coupled atmosphere/biome models, *Climate Dynamics*, *16*(9), 643–659.

de Noblet-Ducoudré, N., J.-P. Boisier, A. Pitman, G. Bonan, V. Brovkin, F. Cruz, C. Delire, V. Gayler, B. Van den Hurk, P. Lawrence, et al. (2012), Determining robust impacts of land-use-induced land cover changes on surface climate over north america and eurasia: results from the first set of lucid experiments, *Journal of Climate*, *25*(9), 3261–3281.

Dirmeyer, P. A. (2011), The terrestrial segment of soil moisture–climate coupling, *Geophysical Research Letters*, *38*(16).

Dirmeyer, P. A., and J. Shukla (1994), Albedo as a modulator of climate response to tropical deforestation, *Journal of Geophysical Research: Atmospheres*, *99*(D10), 20,863–20,877.

Donohoe, A., J. Marshall, D. Ferreira, and D. Mcgee (2013), The relationship between itcz location and cross-equatorial atmospheric heat transport: From the seasonal cycle to the last glacial maximum, *Journal of Climate*, *26*(11), 3597–3618.

Eltahir, E. A. B. (1996), Role of vegetation in sustaining large-scale atmospheric circulations in the tropics, *Journal of Geophysical Research: Atmospheres*, *101*(D2), 4255–4268.

Foley, J. A., J. E. Kutzbach, M. T. Coe, and S. Levis (1994), Feedbacks between climate and boreal forests during the Holocene epoch, *Nature*, *371*, 52–54.

Fu, Q., and K. N. Liou (1993), Parameterization of the radiative properties of cirrus clouds, *Journal of the Atmospheric Sciences*, *50*(13), 2008–2025.

Houldcroft, C. J., W. M. F. Grey, M. Barnsley, C. M. Taylor, S. O. Los, and P. R. J. North (2009), New vegetation albedo parameters and global fields of soil background albedo derived from MODIS for use in a climate model, *Journal of Hydrometeorology*, *10*(1), 183–198.

Kang, S. M., I. M. Held, D. M. Frierson, and M. Zhao (2008), The response of the itcz to extratropical thermal forcing: Idealized slab-ocean experiments with a gcm, *Journal of Climate*, *21*(14), 3521–3532.

Kato, S., N. G. Loeb, F. G. Rose, D. R. Doelling, D. A. Rutan, T. E. Caldwell, L. Yu, and R. A. Weller (2013), Surface irradiances consistent with CERES-derived top-of-atmosphere shortwave and longwave irradiances, *Journal of Climate*, *26*(9), 2719–2740.

Kitoh, A., K. Yamazaki, and T. Tokioka (1988), Influence of soil moisture and surface albedo changes over the African tropical rain forest on summer climate investigated with the MRI GCM-I, *Journal of the Meteorological Society of Japan*, *66*(1), 65–86.

Knorr, W., and K.-G. Schnitzler (2006), Enhanced albedo feedback in North Africa from possible combined vegetation and soil-formation processes, *Climate Dynamics*, *26*(1), 55–63.

Knorr, W., K.-G. Schnitzler, and Y. Govaerts (2001), The role of bright desert regions in shaping North African climate, *Geophysical Research Letter*, *28*(18), 3489–3492.

Kumar, P., B. K. Bhattacharya, R. Nigam, C. M. Kishtawal, and P. K. Pal (2014), Impact of Kalpana-1 derived land surface albedo on short-range weather forecasting over the Indian subcontinent, *Journal of Geophysical Research: Atmospheres*, *119*(6), 2764–2780, doi:10.1002/2013JD020534.

Kutzbach, J., J. Bonan, G .and Foley, S. P. Harrison, et al. (1996), Vegetation and soil feedbacks on the response of the African monsoon to orbital forcing in the early to middle Holocene, *Nature*, *384*(6610), 623–626.

Laval, K., and L. Picon (1986), Effect of a change of the surface albedo of the Sahel on climate, *Journal of the Atmospheric Sciences*, *43*(21), 2418–2429.

Levis, S., G. B. Bonan, and C. Bonfils (2004), Soil feedback drives the mid-Holocene North African monsoon northward in fully coupled CCSM2 simulations with a dynamic vegetation model, *Climate Dynamics*, *23*(7-8), 791–802.

Li, Y., T. Wang, Z. Zeng, S. Peng, X. Lian, and S. Piao (2016), Evaluating biases in simulated land surface albedo from cmip5 global climate models, *Journal of Geophysical Research: Atmospheres*.

Matthes, J. H., S. Goring, J. W. Williams, and M. C. Dietze (2016), Benchmarking historical cmip5 plant functional types across the upper midwest and northeastern united states, *Journal of Geophysical Research*, *121*(2), 523–535.

Nie, J., W. R. Boos, and Z. Kuang (2010), Observational evaluation of a convective quasi-equilibrium view of monsoons, *Journal of Climate*, *23*(16), 4416–4428.

Pierrehumbert, R. T. (2010), 5: Scattering, in *Principles of Planetary Climate*, edited by R. T. Pierrehumbert, pp. 316–385, Cambridge University Press.

Qu, X., and A. Hall (2006), Assessing snow albedo feedback in simulated climate change, *Journal of Climate*, *19*(11), 2617–2630.

Randall, D. A., R. D. Cess, J. P. Blanchet, S. Chalita, R. Colman, D. A. Dazlich, A. D. Del Genio, E. Keup, A. Lacis, H. Le Treut, et al. (1994), Analysis of snow feedbacks in 14 general circulation models, *Journal of Geophysical Research*, *99*(D10), 20,757–20,771.

Samson, G., S. Masson, F. Durand, P. Terray, S. Berthet, and S. Jullien (2016), Roles of land surface albedo and horizontal resolution on the indian summer monsoon biases in a coupled ocean–atmosphere tropical-channel model, *Climate Dynamics*, pp. 1–24.

Schurgers, G., U. Mikolajewicz, M. Gröger, E. Maier-Reimer, M. Vizcaíno, and A. Winguth (2007), The effect of land surface changes on Eemian climate, *Climate dynamics*, *29*(4), 357–373.

Song, J. (1998), Diurnal asymmetry in surface albedo, *Agricultural and Forest Meteorology*, *92*(3), 181–189.

Sperber, K. R., H. Annamalai, I. S. Kang, A. Kitoh, A. Moise, A. Turner, B. Wang, and T. Zhou (2013), The Asian summer monsoon: an intercomparison of CMIP5 vs. CMIP3 simulations of the late 20th century, *Climate Dynamics*, *41*(9-10), 2711–2744.

Sud, Y. C., and M. Fennessy (1982), A study of the influence of surface albedo on July circulation in semi-arid regions using the GLAS GCM, *Journal of Climatology*, *2*(2), 105–125.

Taylor, K. E., R. J. Stouffer, and G. A. Meehl (2009), A summary of the CMIP5 experiment design, *Program For Climate Model Diagnosis and Intercomparison*, *33*.

Taylor, K. E., R. J. Stouffer, and G. A. Meehl (2012), An overview of CMIP5 and the experiment design, *Bulletin of the American Meteorological Society*, *93*(4), 485–498.

Vamborg, F. S. E., V. Brovkin, and M. Claussen (2011), The effect of a dynamic background albedo scheme on Sahel/Sahara precipitation during the mid-Holocene, *Climate of the Past*, *7*(1), 117–131.

Vamborg, F. S. E., V. Brovkin, and M. Claussen (2014), Background albedo dynamics improve simulated precipitation variability in the sahel region, *Earth System Dynamics*, *5*(1), 89.

Walker, J., and P. R. Rowntree (1977), The effect of soil moisture on circulation and rainfall in a tropical model, *Quarterly Journal of the Royal Meteorological Society*, *103*(435), 29–46.

Wang, L., J. N. Cole, P. Bartlett, D. Verseghy, C. Derksen, R. Brown, and K. Salzen (2016), Investigating the spread in surface albedo for snow-covered forests in cmip5 models, *Journal of Geophysical Research: Atmospheres*, *121*(3), 1104–1119.

Xue, Y., and J. Shukla (1993), The influence of land surface properties on Sahel climate. Part 1: desertification, *Journal of climate*, *6*(12), 2232–2245.

Zeng, N., and J. D. Neelin (1999), A land-atmosphere interaction theory for the tropical deforestation problem, *Journal of Climate*, *12*(3), 857–872.

Zeng, N., J. D. Neelin, K.-M. Lau, and C. J. Tucker (1999), Enhancement of interdecadal climate variability in the Sahel by vegetation interaction, *Science*, *286*(5444), 1537–1540.

Zheng, X., and E. A. B. Eltahir (1998), The role of vegetation in the dynamics of West African monsoons, *Journal of Climate*, *11*(8), 2078–2096.

Corresponding author: Xavier J. Levine, Department of Geology and Geophysics, Yale University, New Haven, Connecticut, USA. (xavier.levine@yale.edu)

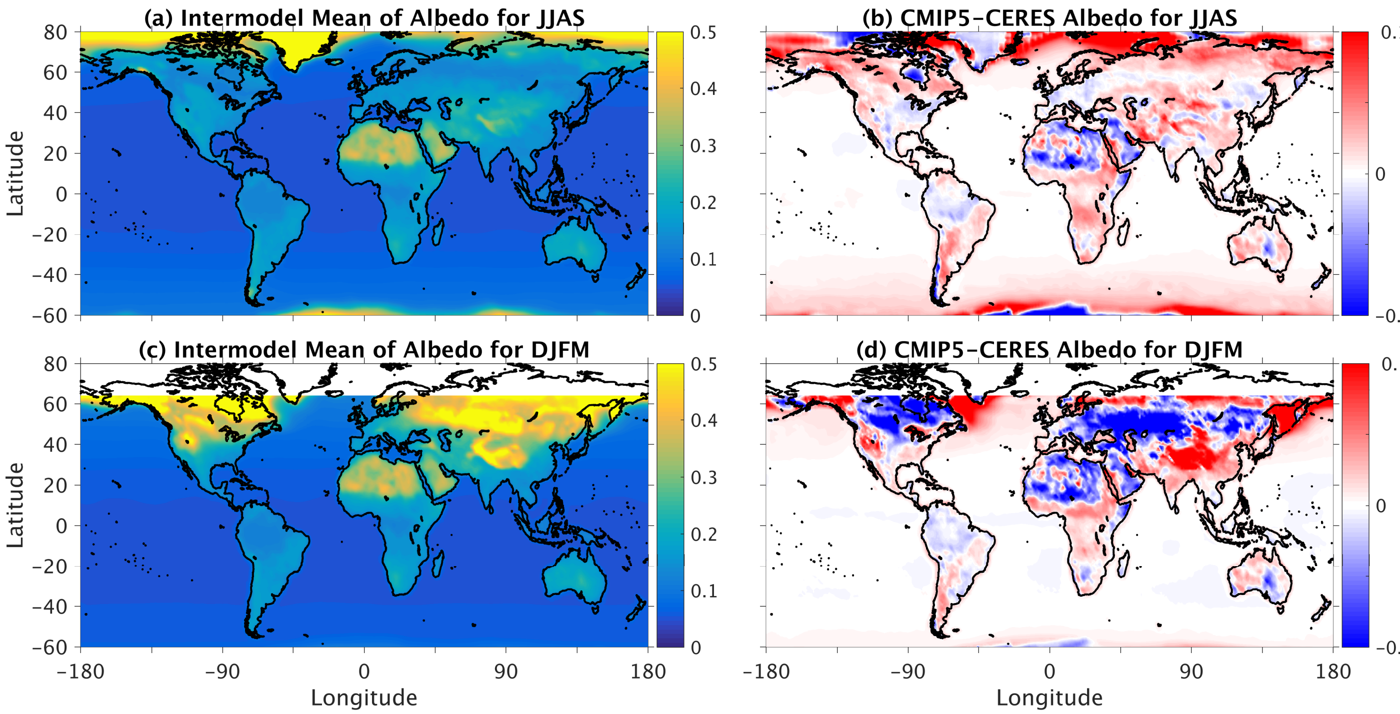

Figure 1. (a) CMIP5 ensemble mean of surface broadband shortwave albedo, averaged over the June-July-August-September season (abbrv. as albedo); CMIP5 albedo is averaged over last 2 decades of the historical run (1985 to 2004). (b) Albedo anomalies in the CMIP5 ensemble mean JJAS albedo (shown on (1a)) with respect to the multi-year mean JJAS albedo retrieved from CERES product; CERES albedo is averaged over the entire measurement window (2005 to 2015). (c) Same as (a) but for the December-January-February-March season (DJFM). (d) Same as (b) but for DJFM.

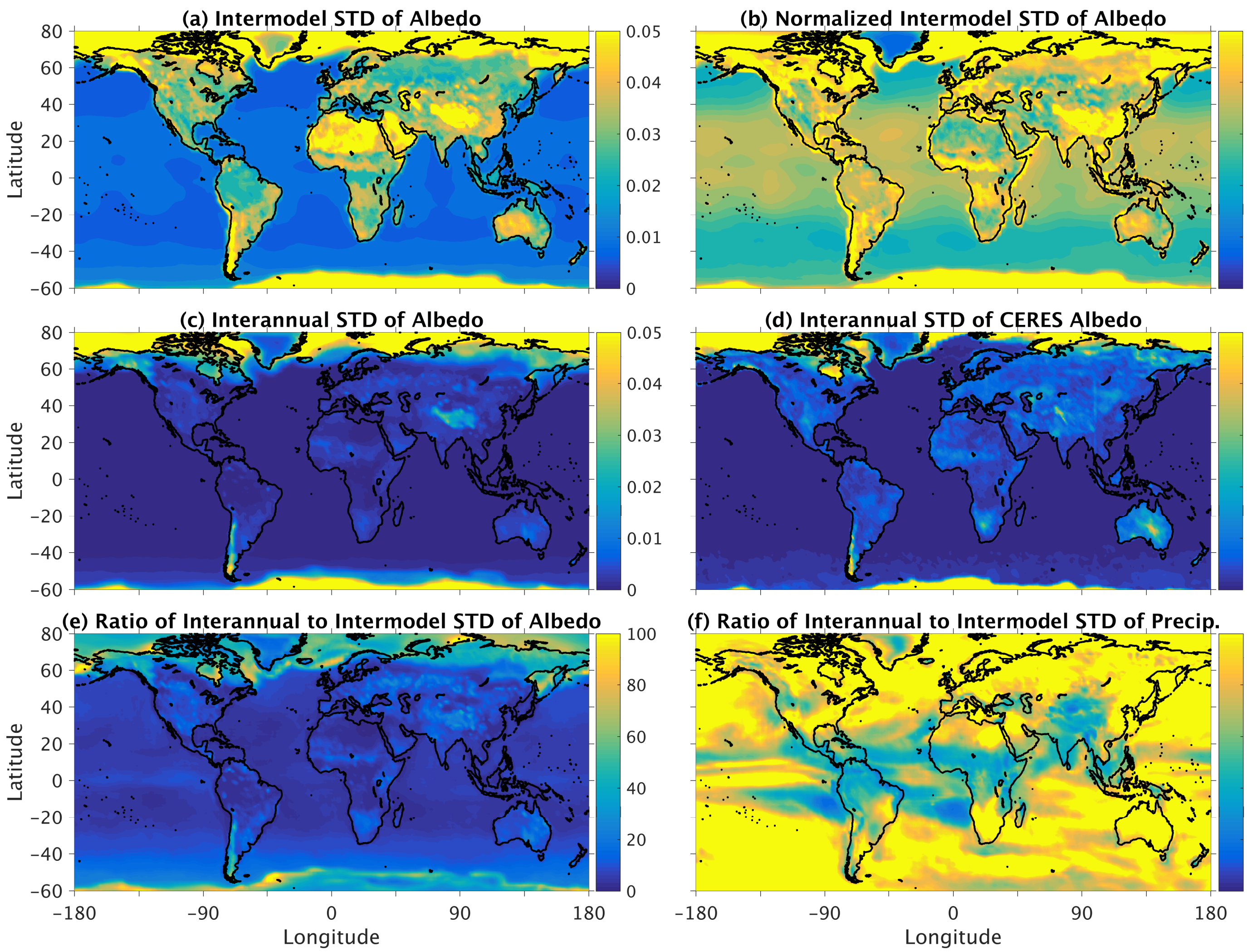

Figure 2. (a) Intermodel standard deviation of albedo in CMIP5 simulations. (b) Normalized intermodel standard deviation of albedo in CMIP5 simulations. (c) Interannual standard deviation of albedo in CMIP5 simulations (1984-2004). (d) Interannual standard deviation of albedo in CERES (2005-2015). (e) Ratio of interannual to intermodel standard deviation of albedo in CMIP5 (in %). (f) Same as in (e) but for precipitation.

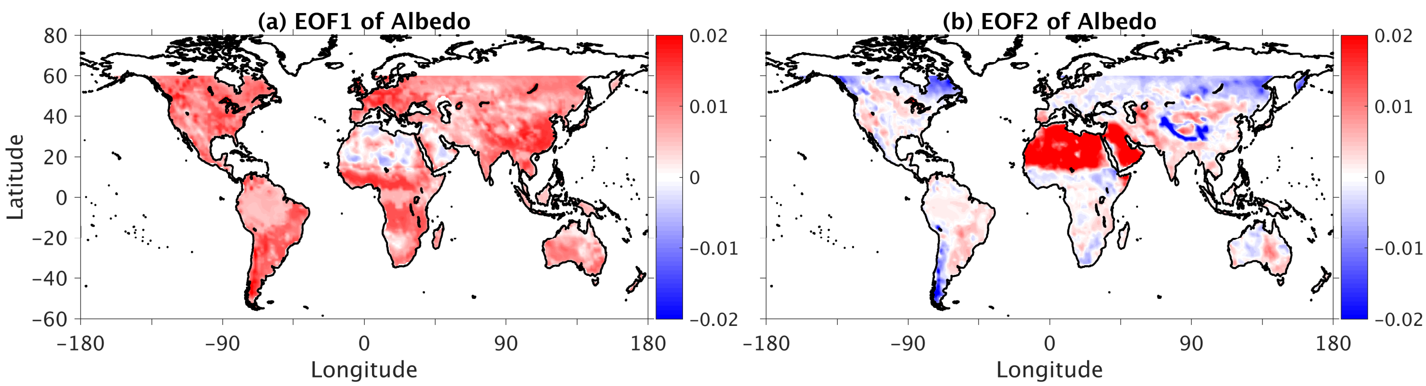

Figure 3. (a) First EOF of JJAS albedo across all CMIP5 simulations; (b) second EOF of JJAS albedo across all CMIP5 simulations. EOF1 explains about 35% of global variance, and EOF2 17%; Higher EOFs explains at most 7%. Same seasonal and multi-year averaging as in Fig.1.

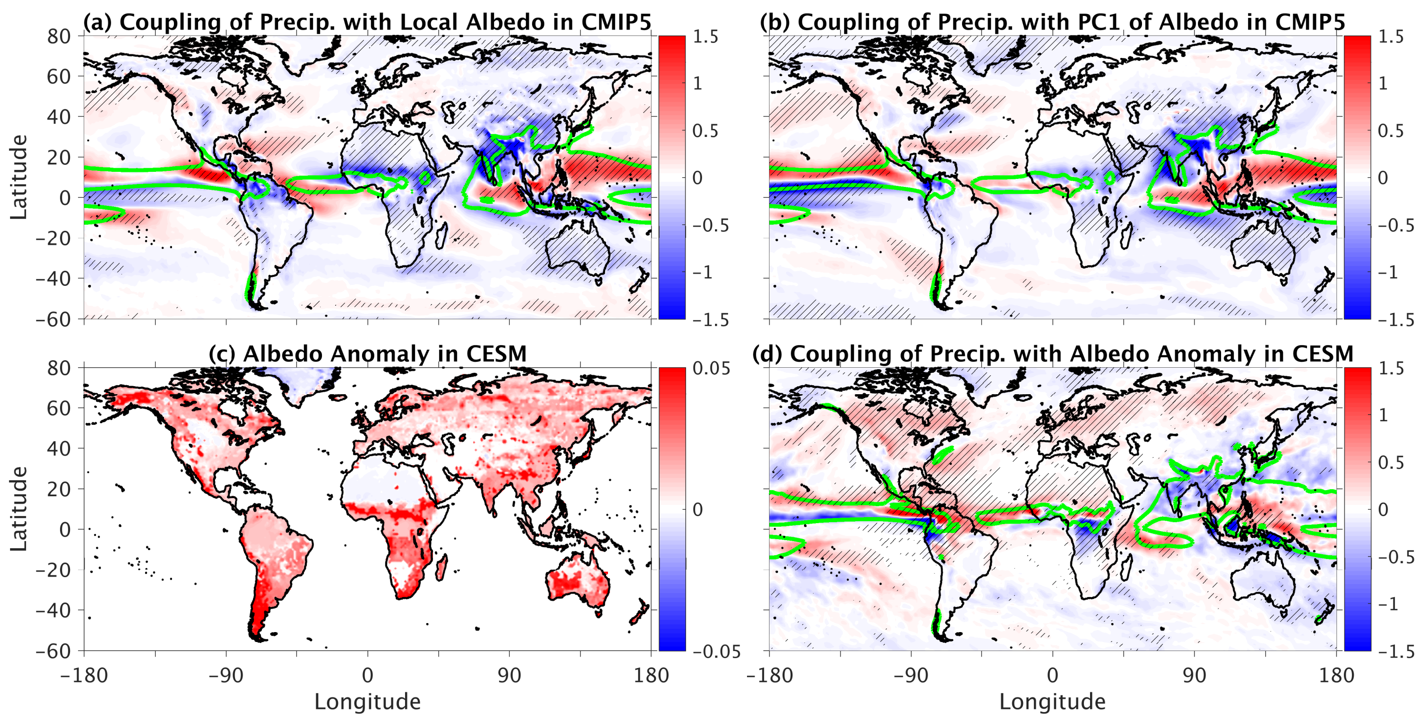

Figure 4. (a) Coupling of precipitation with local albedo anomaly during JJAS season. Areas of high statistical significance ($p < 0.05$) are hatched. (b) Coupling of precipitation in CMIP5 with the global albedo anomaly explained by its PC1 for JJAS. (c) Coupling of precipitation with global albedo anomaly in CESM for JJAS; here, anomaly is defined relative. (c) Prescribed albedo anomaly in CESM in JJAS. (d) Coupling of precipitation with global albedo anomaly in CESM for JJAS; areas of high statistical significance are hatched. Anomaly is defined relative to the CMIP5 ensemble-mean for panels (a) and (b), and relative to a CESM control run forced by present-day climate albedo for panels (c) and (b). Thick green lines in (b) and (d) show the 6 mm day^{-1} precipitation isopleth for ensemble-mean CMIP5 and in control CESM simulation respectively.

Supporting Information for "Land surface albedo bias in climate models and its association with tropical rainfall"

Xavier J. Levine,[1] and William R. Boos[1]

Contents of this file

1. Observational datasets
2. Maximum Covariance Analysis
3. R^2 analysis
4. Figures S1, S2 and S3
5. Tables S1

Corresponding author: Xavier J. Levine, Department of Geology and Geophysics, Yale University, New Haven, Connecticut, USA. (xavier.levine@yale.edu)

[1]Department of Geology and Geophysics,

Yale University, New Haven, Connecticut,

USA.

Introduction

In this supplementary file, we first describe MODIS and SRB as alternate source for the broadband shortwave surface albedo (abbr.. as albedo); albedo distribution inferred from MODIS and SRB are compared to CERES, the observational product used in the main text, and to the CMIP5 ensemble-mean.

We then describe results from a Maximum Covariance Analysis (MCA), a technique that quantifies both local and remote interaction of albedo with precipitation globally. Spatial patterns of co-variability for albedo and rainfall are compared to coupling of precipitation with local albedo and PC1 albedo described in the main text.

At last, we show the local R^2 values for the regression of precipitation on PC1 albedo, to quantify the amount of intermodel variance in precipitation that could be explained potentially from the intermodel variability of PC1 albedo. Similarly, we show the regression of precipitation averaged over continental South Asia with PC1 albedo, to demonstrate that this relationship hold on regional scale as well over the Asian monsoon region.

Observational datasets

While a large regional bias in albedo exists between the ensemble-mean CMIP5 historical simulations and the CERES observational product, we determine whether its regional pattern is robust when comparing CMIP5 to 2 other observational products, MODIS and SRB. While MODIS, SRB and CERES are not strictly independent of each other, surface albedo or shortwave flux outputs are computed using distinct methodologies. We briefly describe each dataset below, and compare the spatial distribution and interannual variability of albedo in MODIS and SRB to CERES and the CMIP5 ensemble-mean.

MODIS: MCD43GF is a gridded dataset of albedo derived from Moderate Resolution Imaging Spectroradiometer (MODIS) instrument on board of the Terra and Aqua platforms. MCD43GF provides a snow-free estimate of surface albedo at $0.05° \times 0.05°$ spatial resolution and 8 days temporal resolution, from 2001 to 2015. This data product is freely available on Prof. Crystal Schaaf's website at University of Massachusetts, Boston. Unlike the original MODIS data provided by NASA, MCD43GF uses a gap filling algorithm to obtain surface albedo over regions obstructed by clouds, and thus allowing for a near global (70°S to 70°N) and continuous coverage of surface albedo over 15 years. Gap filling is critical for acquiring robust statistics over areas covered by clouds during extensive periods of time, an issue prevalent over many tropical regions (e.g. South Asia during boreal summer). MCD43GF provides broadband surface albedo under white-sky (isotropic, diffuse illumination) and black sky albedo (single beam illumination at local noon); these broadband values are obtained from measurements of surface reflectance over 7 specific windows in the visible and near-infrared range of the shortwave spectrum by the MODIS instrument [*Schaaf et al.*, 2011]. Albedo bias between the ensemble-mean CMIP5 albedo and MODIS white-sky albedo bias are found to be very similar to those between CMIP5 and CERES (compare Fig. S1a with 1b) during JJAS, with negative bias over the Sahara and Arabian deserts, and positive biases over most of the other land regions. Furthermore, the interannual standard deviation in albedo show similar values in MODIS and CERES, pointing to the broad consistency among both datasets (Fig. S1c).

SRB-GEWEX: The NASA/GEWEX Surface Radiation Budget (SRB) project provides a gridded dataset of monthly mean longwave and shortwave fluxes at the top-of-atmosphere (TOA) and surface, at a horizontal resolution of $1^\circ \times 1^\circ$ for all years between 1984 and 2007. SRB output values for surface broadband shortwave fluxes are computed from a radiative transfer algorithm that relies on TOA shortwave fluxes measured by space-borne observational platforms (NOAA-7, NOAA-9, NOAA-11, NOAA-14, NOAA-16, NOAA-18), cloud profiles inferred from the International Satellite Cloud Climatology Project (ISCCP), and various atmospheric variables output from the GMAO reanalysis dataset (e.g. temperature and moisture profiles) [*Pinker and Laszlo*, 1992]. We use the same methodology to compute albedo as for the CERES dataset or the CMIP5 simulations, that is a seasonal mean of albedo is first obtained by computing albedo as the ratio of monthly-mean broadband shortwave upwelling to downwelling fluxes, before averaging albedo over the boreal summer season. Despite having a better overlap with the time-period of the CMIP5 historical simulations, SRB is generally deemed less desirable than either CERES or MODIS due the large number of platform changes between 1984 and 2007 creating spurious data jumps, as well as its large reliance on reanalysis products. We find large bias in albedo between CMIP5 and SRB, but its spatial pattern shows important deviation from that found between CMIP5 and either CERES or MODIS: while the sign of the anomalies broadly agree over much of the globe, that over Africa is inconsistent: instead of showing negative anomalies over the Sahara and positive anomalies over the rest of the continent, anomalies from SRB are positive over much of the Sahara and negative over most of the rest of Africa (Fig. S1b). The CMIP5 anomaly from SRB over the Tibetan Plateau is also substantially stronger than the anomaly from CERES or MODIS. Further discrepancy is found in the interannual standard deviation, which is substantially larger in SRB than in MODIS or CERES (Fig. S1d). Some of the discrepancies between SRB and either CERES or MODIS could be attributed to spurious instrumental bias in SRB, as evidently shown when comparing the unphysical variation in the interannual standard deviation of albedo in SRB between the Indian sector and the Atlantic sector of the Southern Ocean (Fig. S1d).

Maximum Covariance Analysis

A maximum covariance analysis (MCA) is powerful tool to study remote connection between climatic variables [see *Bretherton et al.*, 1992, for a description of MCA as an exploratory method]. In particular, it can be used to find the dominant mode of interaction between land albedo and precipitation globally. This is done by performing a PCA on the intermodel covariance matrix of albedo with precipitation. The first mode explains about 49% of the variance in the intermodel covariance; its EOF resembles greatly EOF1 of albedo (S2), confirming our earlier assumption that the vegetated regions identified on Fig. 3a are indeed the most likely to interact with precipitation on global scales. Similarly, the PC1 of the covariance matrix, which shows regions where precipitation variance correlates strongly with regions of largest coherent albedo variance (Fig. S2c), corresponds broadly to regions where precipitation is found to couple strongly with PC1 albedo (Fig. 4b). The second mode of the intermodel covariance matrix explains only

21% of its global variance; its EOF resembles EOF2 of albedo (Fig. S2b), consistent with the desert regions identified on Fig. 3b exerting a smaller but non-negligible influence on precipitation; PC2 of the covariance matrix shows that precipitations variability associated with PC2 albedo is qualitatively similar over ocean regions than that associated with PC1 albedo, i.e. a poleward shift of the ITCZ associated with brighter land albedo (Fig. S2d); on the other hand, brighter desert albedo appears to be associated with greater precipitation over some land regions, especially the Indian subcontinent.

R^2 analysis

The amount intermodel variance in precipitation that could potentially be explained from the albedo variability over vegetated regions on a global scale (i.e., EOF1 of albedo, as shown on Fig. 3a) can be quantified by the R^2 value of the regression (Fig. S3a), if assuming that albedo variability causes precipitation variability, as suggested by our study Over regions where precipitation is correlated with PC1 albedo (e.g. Western Pacific, South Asia, Australia, etc), local R^2 values suggest that intermodel albedo variability could explain between 20% and 50% of the total intermodel variance of precipitation (Fig. S3a). The coupling of precipitation with albedo can be strong on regional scale as well; this is true when regressing precipitation over the South Asia continent (here, South Asia is defined as all land areas contained in the $60° - 180°$E longitudinal sector and $5° - 45°$N latitudinal band) on PC1 albedo (Fig. S3b), where up to half of the intermodel variance in precipitation could potentially be explained from the global variability of albedo over vegetated areas (i.e. PC1 albedo) .

References

Bretherton, C. S., C. Smith, and J. M. Wallace (1992), An intercomparison of methods for finding coupled patterns in climate data, *Journal of climate*, *5*(6), 541–560.

Pinker, R. T., and I. Laszlo (1992), Modeling surface solar irradiance for satellite applications on a global scale, *Journal of Applied Meteorology*, *31*(2), 194–211.

Schaaf, C. L. B., J. Liu, F. Gao, and A. H. Strahler (2011), MODIS albedo and reflectance anisotropy products from Aqua and Terra.

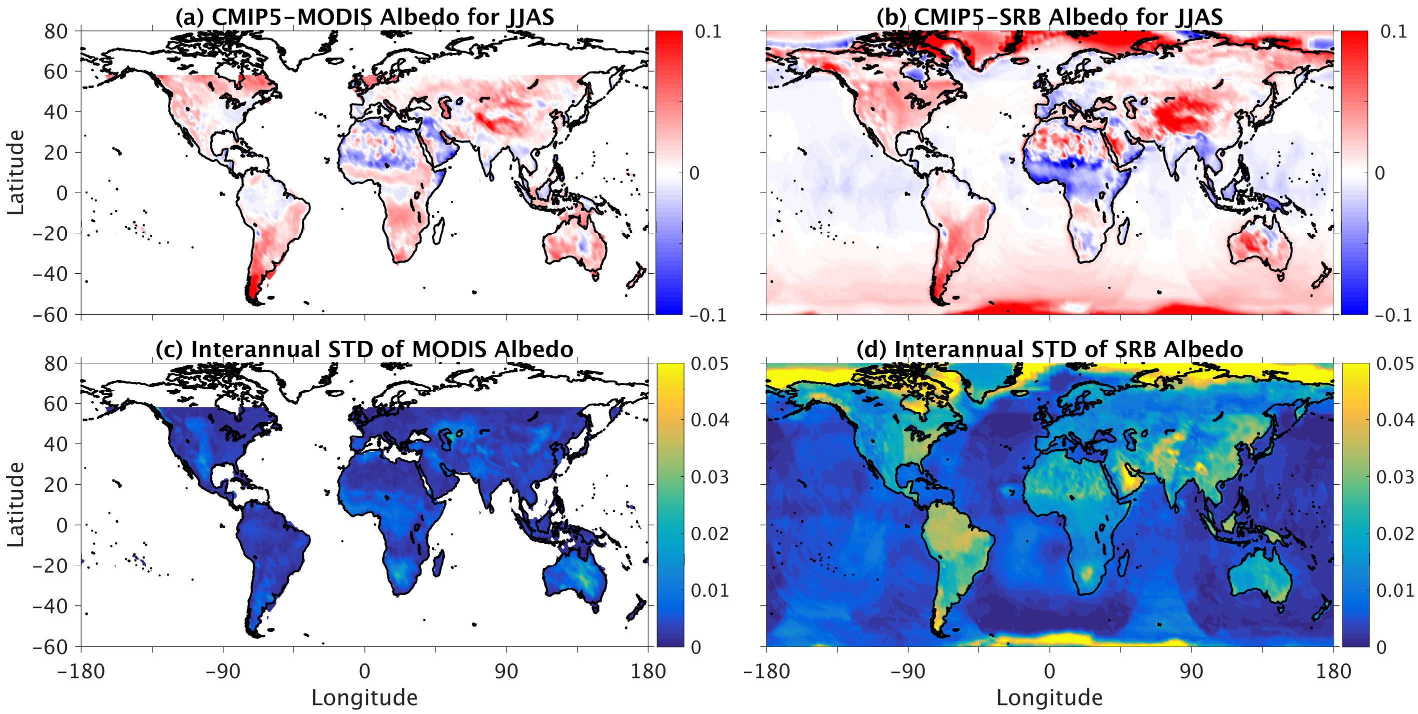

Figure S1. (a) CMIP5 albedo anomalies during JJAS with respect to MODIS. (b) CMIP5 albedo anomalies during JJAS with respect to SRB/GEWEX. MODIS albedo for JJAS is averaged over the 2001 to 2015 period, and SRB over the 1985 to 2004 period. (c) Interannual standard deviation of albedo in MODIS. (d) Interannual standard deviation of albedo in SRB.

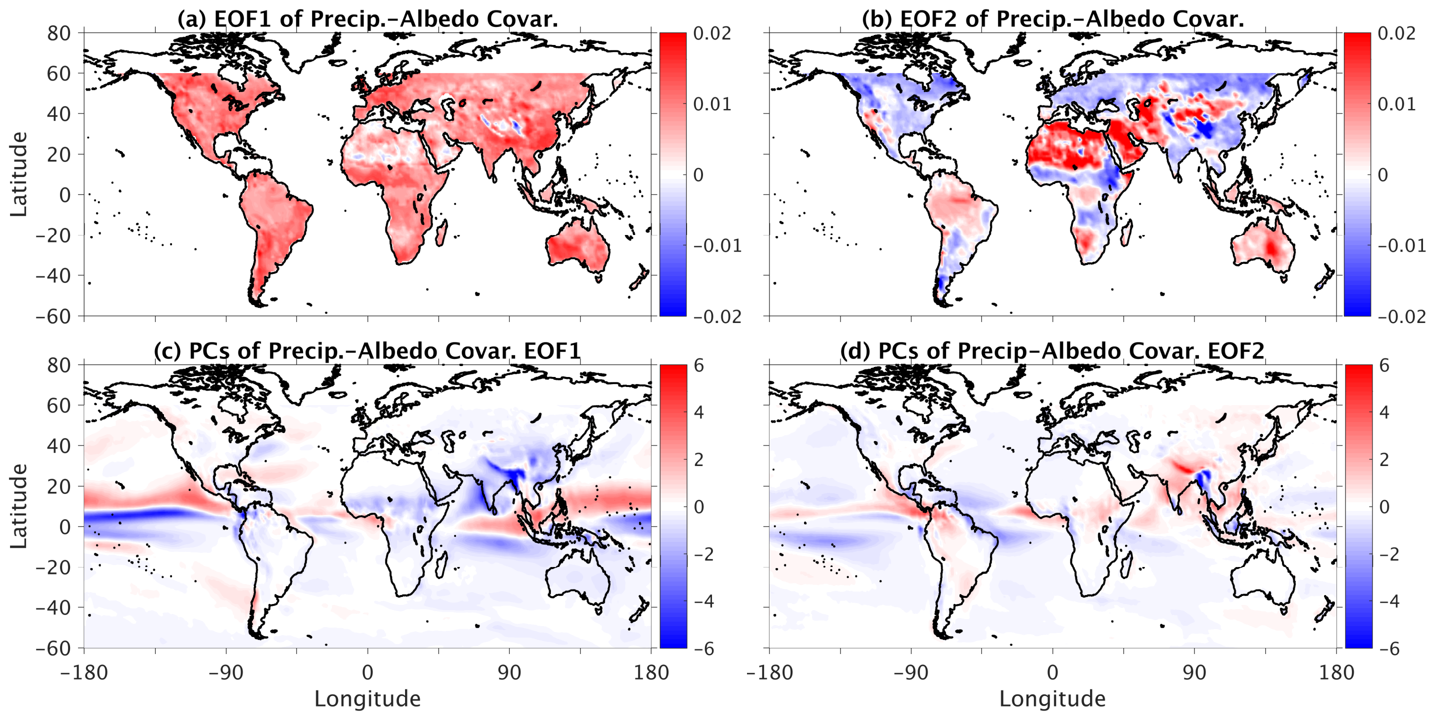

Figure S2. (a) First EOF of the precipitation-albedo covariance matrix. (b) Second EOF of the precipitation-albedo covariance matrix. (c) PCs of the First EOF of the precipitation-albedo covariance matrix. (d) PCs of the Second EOF of the precipitation-albedo covariance matrix. EOF1 explains about 49% of global variance, and EOF2 21%; Higher EOFs explains at most 8%. Same seasonal and multi-year averaging as in Fig.1.

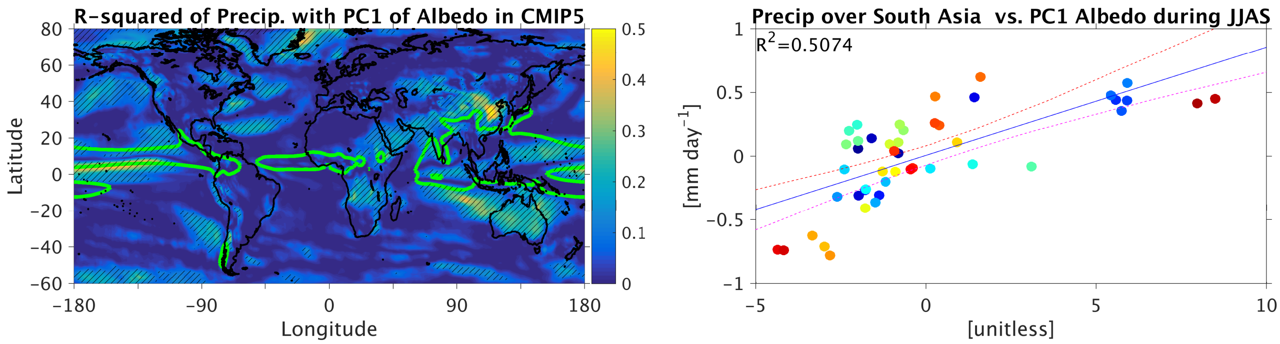

Figure S3. (a) R^2 value of the regression of local precipitation with PC1 albedo; hatching shows area where regression is statistically significant ($p \leq 0.05$), and green line the 6 mm day^{-1} precipitation isopleth. (b) Regression of the precipitation anomaly (from its ensemble-mean value) averaged continental South Asia with PC1 albedo; solid blue line shows the mean regression slope, and dashed lines show the 95% confidence interval on the slope. Continental South Asia is defined as the land areas contained in the 60° − 180°E longitudinal sector and 5° − 45°N latitudinal band.

Table S1. List of GCMs and Observational Products

Index	Name	Resl	albedo	rainfall
A	CERES	$1.0000° \times 1.0000°$	Y	**N**
B	MODIS	$0.0500° \times 0.0500°$	Y	**N**
C	SRB	$1.0000° \times 1.0000°$	Y	**N**
1	ACCESS1-0	$1.8750° \times 1.2500°$	Y	Y
2	ACCESS1-3	$1.8750° \times 1.2500°$	Y	Y
3	BCC-CSM1-1	$2.8125° \times 2.7906°$	Y	Y
4	BCC-CSM1-1-m	$1.1250° \times 1.1215°$	Y	Y
5	BNU-ESM	$2.8125° \times 2.7906°$	Y	Y
6	CanCM4	$2.8125° \times 3.1476°$	Y	Y
7	CanESM2	$2.8125° \times 3.1476°$	Y	Y
8	CCSM4	$1.2500° \times 0.9424°$	Y	Y
9	CESM1-BGC	$1.2500° \times 0.9424°$	Y	Y
10	CESM1-CAM5	$1.2500° \times 0.9424°$	Y	Y
11	CESM1-FASTCHEM	$1.2500° \times 0.9424°$	Y	Y
12	CESM1-WACCM	$2.5000° \times 1.8947°$	Y	Y
13	CMCC-CESM	$3.7500° \times 4.1746°$	Y	Y
14	CMCC-CM	$0.7500° \times 0.8371°$	Y	Y
15	CMCC-CMS	$1.8750° \times 2.1037°$	Y	Y
16	CNRM-CM5	$1.4062° \times 1.5800°$	Y	Y
17	CNRM-CM5-2	$1.4062° \times 1.5800°$	Y	Y
18	CSIRO-Mk3-6-0	$1.8750° \times 2.1039°$	Y	Y
19	FGOALS-g2	$2.8125° \times 4.8855°$	Y	Y
20	FIO-ESM	$2.8125° \times 2.7906°$	Y	Y
21	GFDL-CM2p1	$2.5000° \times 2.0225°$	Y	Y
22	GFDL-CM3	$2.5000° \times 2.0000°$	Y	Y
23	GFDL-ESM2G	$2.5000° \times 2.0225°$	Y	Y
24	GFDL-ESM2M	$2.5000° \times 2.0225°$	Y	Y
25	GISS-E2-H	$2.5000° \times 2.0000°$	Y	Y
26	GISS-E2-H-CC	$2.5000° \times 2.0000°$	Y	Y
27	GISS-E2-R	$2.5000° \times 2.0000°$	Y	Y
28	GISS-E2-R-CC	$2.5000° \times 2.0000°$	Y	Y
29	HadCM3	$3.7500° \times 2.5000°$	Y	Y
30	HadGEM2-AO	$1.8750° \times 1.2500°$	**N**	Y
31	HadGEM2-CC	$1.8750° \times 1.2500°$	Y	Y
32	HadGEM2-ES	$1.8750° \times 1.2500°$	Y	Y
33	inmcm4	$2.0000° \times 1.5000°$	Y	Y
34	IPSL-CM5A-LR	$3.7500° \times 1.8947°$	Y	Y
35	IPSL-CM5A-MR	$2.5000° \times 1.2676°$	Y	Y
36	IPSL-CM5B-LR	$3.7500° \times 1.8947°$	Y	Y
36	MIROC4h	$0.5625° \times 0.6282°$	Y	Y
38	MIROC5	$1.4062° \times 1.5668°$	Y	Y
39	MIROC-ESM-CHEM	$2.8125° \times 3.1215°$	Y	Y
40	MIROC-ESM	$2.8125° \times 3.1215°$	Y	Y
41	MPI-ESM-MR	$1.8750° \times 2.1039°$	Y	Y
42	MPI-ESM-P	$1.8750° \times 2.1039°$	Y	Y
43	MPI-ESM-LR	$1.8750° \times 2.1039°$	Y	Y
44	MRI-CGCM3	$1.1250° \times 1.2649°$	Y	Y
45	MRI-ESM1	$1.1250° \times 1.2649°$	Y	Y
46	NorESM1-ME	$2.5000° \times 1.8947°$	Y	Y
47	NorESM1-M	$2.5000° \times 1.8947°$	Y	Y